

LIGHT PARTICLE EMISSION IN FUSION-LIKE $^{14}\text{N} + ^{197}\text{Au}$ COLLISIONS AT $E/A = 35$ MeV

Z. CHEN, C.K. GELBKE, J. POCHODZALLA¹, C.B. CHITWOOD², D.J. FIELDS³, W.G. GONG,
W.G. LYNCH and M.B. TSANG

*Department of Physics and National Superconducting Cyclotron Laboratory, Michigan State University,
East Lansing, MI 48824, USA*

Received 23 February 1987
(Revised 1 June 1987)

Abstract: Single- and two-particle inclusive cross sections for light nuclei (p, d, t, ^3He , $^6\text{-}^9\text{Li}$, $^7,8,10\text{Be}$) were measured for ^{14}N induced reactions on ^{197}Au at $E/A = 35$ MeV. At forward angles, $\theta \approx 20^\circ$, quasi-elastic peripheral reactions and more violent fusion-like collisions were discriminated by measuring the folding angle between two coincident fission fragments resulting from the decay of the heavy reaction residue. More pronounced correlation functions, but very similar emission temperatures are observed for fusion-like collisions as compared to peripheral collisions.

E NUCLEAR REACTIONS $^{197}\text{Au}(^{14}\text{N}, \text{X})$, ($^{14}\text{N}, \text{F}$), $E = 35$ MeV/nucleon; measured (particle)(particle) correlations, fission (fragment)(fragment)-coin, inclusive σ for $\text{X} = \text{p}, \text{d}, \text{t}, ^3\text{He}, ^6,7,8,9\text{Li}, ^7,8,10\text{Be}$; deduced source dimensions, emission temperatures.

1. Introduction

For intermediate energy nucleus-nucleus collisions, particle emission during the equilibration stages of the reaction is important, rendering a description of the reaction in terms of the classical concept of compound nucleus formation and decay inappropriate. In the absence of detailed dynamical treatments of the spatial and temporal evolution of the collision process, recourse is often taken in models based on the assumption of statistical particle emission from nuclear subsets characterized by their average velocity, space-time extent, and excitation energy or "temperature"¹⁻⁷). Experimental information about the temperatures and the space-time evolution of such subsystems is clearly needed. While inclusive measurements can provide insights about the average properties of the emitting system, more detailed information must be obtained from measurements in which specific classes of reactions can be suppressed or enhanced.

The extraction of nuclear temperatures from the kinetic energy spectra of the emitted particles⁸) can be complicated by the effects of collective motion⁹), the

¹ Present address: Institut für Kernphysik, J.W. Goethe Universität, 6000 Frankfurt 90, W. Germany.

² Present address: Coleman Research, 4946 Research Dr. N.W., Huntsville, AL35805, USA.

³ Present address: Chemistry Division, Lawrence Livermore National Laboratory, P.O. Box 808, Livermore, CA 94550, USA.

temporal evolution of the emitting system^{6,10,11}), the sequential decay of highly excited primary fragments¹⁰), and fluctuations of the Coulomb barrier¹²). Alternatively, if the emitting (sub)system is close to chemical equilibrium, information about its excitation energy density or temperature can be extracted from the relative populations of states¹³⁻²⁰). The relative populations of particle unbound states can be determined by measuring two-particle correlations at small relative momenta. In addition, such measurements provide information about the space-time characteristics of the emitting system²¹⁻³⁶).

In order to obtain more detailed experimental information about emission temperatures and source dimensions for different classes of reactions we measured single- and two-particle distributions in coincidence with two fission fragments resulting from the decay of heavy reaction residues. In addition, we measured single- and two-particle inclusive distributions over the angular range of $\theta_{\text{lab}} \approx 10^\circ - 70^\circ$. Quasi-elastic and more violent, fusion-like projectile-target interactions were discriminated by the linear momentum transfer to the heavy reaction residue by measuring the folding angle between two coincident fission fragments. Some of the results of this series of experiments have already been published^{19,35-37}). Experimental details are given in the following section. Single-particle inclusive distributions are presented in sect. 3. Sect. 4 gives a simplified discussion of the information content of two-particle correlations. Two-particle inclusive correlation measurements will be discussed in sect. 5. Single- and two-particle distributions measured in coincidence with two fission fragments will be discussed in sects. 6 and 7. Summary and conclusions will be given in sect. 8.

2. Experimental details

The experiment was performed at the National Superconducting Cyclotron Laboratory at Michigan State University. Gold targets of 1.1, 10, and 19 mg/cm² areal density were irradiated with ¹⁴N ions of $E/A = 35$ MeV incident energy. Light particles ($Z \leq 3$) were detected by a close packed hexagonal array of 13 $\Delta E - E$ telescopes, each consisting of a 400 μm thick Si detector and a 10 cm thick NaI detector. Each telescope subtended a solid angle of 0.94 msr; the angular separation between adjacent detectors was 6.1°.

Single and two-particle inclusive measurements were performed with the center of the hodoscope positioned at the angles of $\theta_{\text{av}} = 20^\circ$, 35° and 50° with respect to the beam axis; for these measurements a thick (19 mg/cm²) gold target was used. Measurements in coincidence with fission fragments were performed with the center of the hodoscope positioned at $\theta_{\text{av}} = 20^\circ$; for these measurements a thin (1.1 mg/cm²) gold target was used.

Coincident fission fragments were detected with two xy -position sensitive parallel plate detectors with individual active areas of $11 \times 11 \text{ cm}^2$. The centers of these detectors were mounted in the plane defined by the center of the light particle

hodoscope and the beam axis. They were positioned at the distances of $d_1 = 13.6$ cm and $d_2 = 17.3$ cm from the target and at the polar angles with respect to the beam axis of $\theta_1 = 95^\circ$ and $\theta_2 = -55^\circ$, respectively.

Single-particle inclusive cross sections for Li and Be fragments were measured in a separate run using two $\Delta E - \Delta E - E$ silicon detector telescopes consisting of detectors of 75 μm , 400 μm , and 5 mm thickness. The solid angles of these telescopes were 2.1 and 4.1 msr; the target thickness was 10 mg/cm².

The energy calibrations of the silicon detectors were performed by injecting known amounts of charge into the preamplifier inputs. The energy calibrations of the NaI detectors were established by scattering alpha particles of 60 and 100 MeV energy from a polyethylene target and detecting the scattered α -particles and recoil protons at various scattering angles. The calibrations are accurate to within 3% for $E/A \leq 25$ MeV and within 2% for $E/A \approx 25-50$ MeV. Gain stabilization procedures similar to those described by ref.¹⁸⁾ were employed.

Coincidences and downscaled singles events were written on magnetic tape and analyzed off-line. In the off-line analysis, energy thresholds of 12, 15, 18, 35, and 40 MeV were used for protons, deuterons, tritons, ³He nuclei, and α -particles, respectively. The coincidence cross sections were corrected for random coincidences. Absolute cross sections were determined from the known target thicknesses, solid angles, and integrated beam currents. They are believed to be accurate to within 15%.

3. Single-particle inclusive cross sections

Single-particle inclusive cross sections for light particles (p, d, t, α) are shown in fig. 1. These cross sections exhibit the characteristic features established for a large number of heavy-ion induced reactions at intermediate energies [see ref.³⁸⁾ for a recent review]. At forward angles, the energy spectra exhibit a broad maximum which is located close to the beam velocity. This peak could be attributed to peripheral break-up reactions. At larger angles, the energy spectra exhibit rather structureless, nearly exponential slopes which are considerably less steep than expected from compound nucleus evaporation. Qualitatively similar energy spectra are observed for the emission of Li and Be fragments, see figs. 2 and 3.

In order to bring these data into context with previous measurements and to provide extrapolations to unmeasured scattering angles and particle energies, the data were fitted by a parametrization employing the superposition of three maxwellian distributions ("moving sources"):

$$\frac{d^2\sigma}{d\Omega dE} = \sum_{i=1}^3 N_i \sqrt{E - U_c} \exp(-[E - U_c + E_i - 2\sqrt{E_i(E - U_c)} \cos \theta]/T_i). \quad (1)$$

Here, U_c is the kinetic energy gained by the Coulomb repulsion from the heavy reaction residue assumed to be stationary in the laboratory system; N_i is a normalization constant and T_i is the "temperature" parameter of the i th sources; $E_i = \frac{1}{2}mv_i^2$,

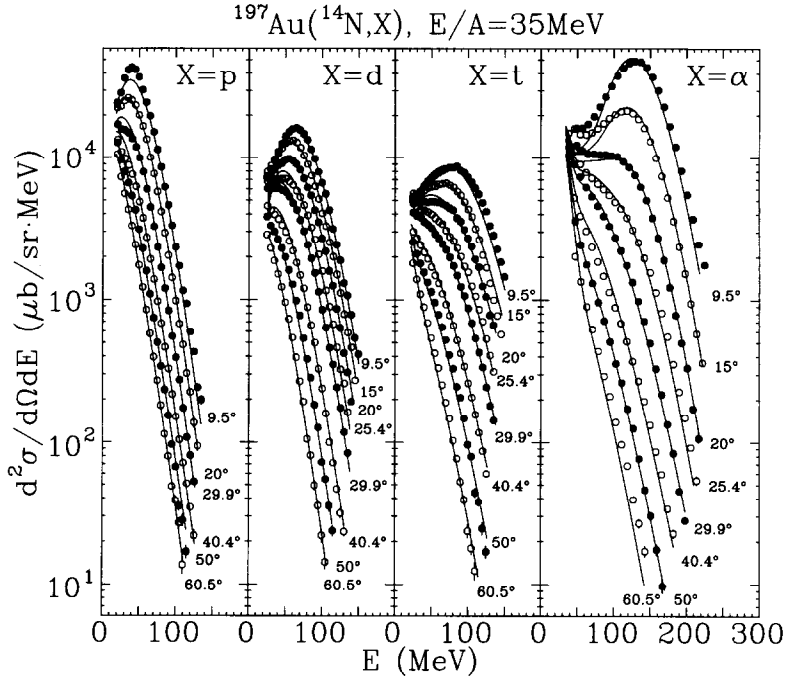


Fig. 1. Differential cross sections for p, d, t, and α -particles. The solid curves show fits with eq. (1). The fit parameters are listed in table 1.

where m is the mass of the emitted particle and v_i is the velocity of the i th source in the laboratory system.

In order to reduce the number of free parameters, the parameters of one source were kept fixed at $v_1 = 0.0185c$ and $T_1 = 5$ MeV. These parameters are consistent with evaporation from fully equilibrated heavy reaction residues formed in incomplete fusion reactions. The remaining parameters were fit to the data. The resulting fits are shown by the solid lines in figs. 1-3; the parameters are listed in table 1. In addition to the slow, “target-like”, and fast, “projectile-like”, sources, an intermediate rapidity source is required to fit the cross sections at large transverse momenta. For light particles (p, d, t, α), the temperature parameters for this source agree with the systematic trends established previously^{4,8,38,39}). It should, however, be kept in mind that the exact values of these parameters depend on the specific choice of parametrization⁴⁰).

4. Two-particle correlations at small relative momenta

The two-particle correlation function, $R(\mathbf{q})$, is defined in terms of the coincidence yield, $Y_{12}(\mathbf{p}_1, \mathbf{p}_2)$, and the single-particle yields, $Y_1(\mathbf{p}_1)$ and $Y_2(\mathbf{p}_2)$:

$$\sum Y_{12}(\mathbf{p}_1, \mathbf{p}_2) = C_{12}(1 + R(\mathbf{q})) \sum Y_1(\mathbf{p}_1) Y_2(\mathbf{p}_2). \quad (2)$$

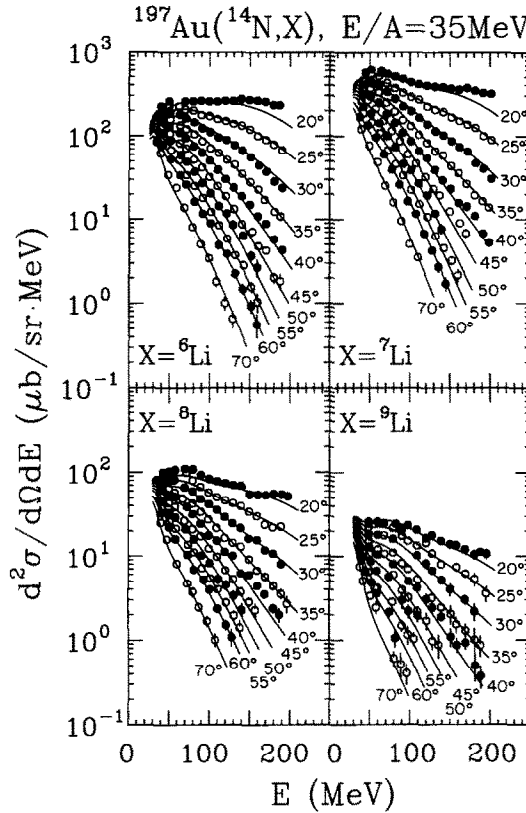


Fig. 2. Differential cross sections for lithium isotopes. The solid curves show fits with eq. (1). The fit parameters are listed in table 1.

Here \mathbf{p}_1 and \mathbf{p}_2 are the laboratory momenta of particles 1 and 2; \mathbf{q} is the momentum of relative motion (non-relativistically, $\mathbf{q} = \mu (\mathbf{p}_2/m_2 - \mathbf{p}_1/m_1)$); C_{12} is a normalization constant which is determined by the requirement that $R(q) = 0$ for large relative momenta. For each gating condition, the sums on both sides of eq. (2) were extended over all energy and detector combinations corresponding to the given bins of \mathbf{q} ; in most cases the correlation functions were determined as a function of $q = |\mathbf{q}|$ only.

Two-particle correlations are sensitive to the space-time extent of the emitting system. This can be understood most easily in the thermal model³⁰). If one assumes that two particles only interact with each other and not with the rest of the system, one may approximate the two-particle density of states as:

$$\rho(P, q) = \rho_0(P) \cdot (\rho_0(q) + \Delta\rho(q)), \quad (3)$$

where $\rho_0(P) = VP^2/2\pi^2$ and $\rho_0(q) = (2s_1 + 1)(2s_2 + 1) Vq^2/2\pi^2$ denote the plane wave densities for the motion of the center-of-mass of the two particles and for their relative motion, respectively; s_1 and s_2 denote the spins of the two particles; V

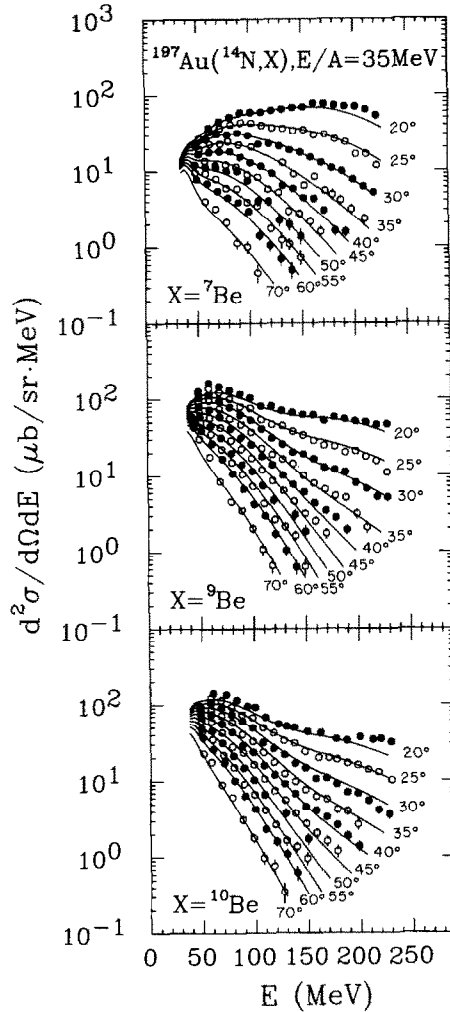


Fig. 3. Differential cross sections for beryllium isotopes. The solid curves show fits with eq. (1). The fit parameters are listed in table 1.

denotes the volume of the system. The neglect of higher order interactions is expected to be reasonable for the final, low-density disintegration stages of the collision. At higher densities, this approximation may be inadequate. For non-identical particles the interaction term, $\Delta\rho(q)$, can be written as:

$$\Delta\rho(q) = \frac{1}{\pi} \sum_{J,\alpha} (2J+1) \frac{\partial \delta_{J,\alpha}}{\partial q}. \tag{4}$$

Here, $\delta_{J,\alpha}$ is the scattering phase shift for channel α and total angular momentum J . Unlike the plane-wave densities, the interaction term does not depend on the size

TABLE 1
Parameters used to fit the single-particle inclusive cross sections shown in figs. 1-3

Particle	U_c (MeV)	T_1 (MeV)	v_1/c	N_1 (a.u.)	T_2 (MeV)	v_2/c	N_2 (a.u.)	T_3 (MeV)	v_3/c	N_3 (a.u.)
p	9.9	5	0.0185	4581	10.0	0.118	5275	5.5	0.248	4990
d	9.6	5	0.0185	1764	10.5	0.122	2131	6.3	0.227	2046
t	9.3	5	0.0185	2794	11.5	0.125	1216	6.4	0.223	901
α	18.1	5	0.0185	24040	11.9	0.123	2514	4.7	0.234	8491
^6Li	26.1	5	0.0185	83.7	14.5	0.099	49.5	12.0	0.210	59.9
^7Li	25.8	5	0.0185	169	13.6	0.086	115	12.7	0.197	86.6
^8Li	25.5	5	0.0185	38.0	14.8	0.084	19.6	12.8	0.190	14.9
^9Li	25.4	5	0.0185	14.6	13.2	0.087	5.72	13.3	0.174	2.67
^7Be	34.1	5	0.0185	8.95	15.7	0.111	9.35	10.2	0.210	25.7
^9Be	33.4	5	0.0185	29.3	13.5	0.077	27.6	12.7	0.188	16.4
^{10}Be	33.2	5	0.0185	32.3	12.8	0.069	27.1	15.6	0.166	7.70

of the system. Eq. (3) can be cast into the form:

$$\rho(P, q) \approx \rho_0(P)\rho_0(q) \cdot (1 + R(q)) = \rho_0(p_1)\rho_0(p_2) \cdot (1 + R(q)). \quad (5)$$

Here, $\rho_0(p_i) = (2s_i + 1) \cdot Vp_i^2/2\pi^2$ denotes the plane wave density of states for particle i , and $R(q)$ is given by:

$$R(q) = \frac{2\pi}{(2s_1 + 1)(2s_2 + 1)Vq^2} \sum_{J, \alpha} (2J + 1) \frac{\partial \delta_{J, \alpha}}{\partial q}. \quad (6)$$

If one assumes, that the singles and coincidence yields are given by thermal equilibrium distributions characterized by a temperature T ,

$$Y_i(p_i) \propto \rho_0(p_i) e^{-E_i/T}, \quad (i = 1, 2), \quad (7)$$

$$Y_{12}(p_1, p_2) \propto \rho(P, q) e^{-(E_1 + E_2)/T}, \quad (8)$$

one can see immediately that $R(q)$ agrees with the definition of eq. (2). Within the thermal model, the two-particle correlation function depends only on the volume of the emitting system. It is independent of the temperature of the system.

Information about the temperature of the system can be obtained by investigating the relative populations of states. As a function of the excitation energy, E , the population of states can be written as

$$\frac{dn(E)}{dE} \propto e^{-E/T} \Delta\rho(E) \approx N e^{-E/T} \sum_i \frac{(2J_i + 1)\Gamma_i/2\pi}{(E - E_i)^2 + \frac{1}{4}\Gamma_i^2}, \quad (9)$$

Here, N is a normalization constant and $\Delta\rho(E)$ denotes the density of states corresponding to the interaction term, eq. (4). The right-hand side is a good approximation if the energy dependence of the phase shifts is dominated by a series of resonances. Expressions similar to eq. (9) can also be derived from alternative

statistical formulations such as appropriate generalizations of evaporative models. The population of states decaying into channel c can be written as

$$\left(\frac{dn(E)}{dE}\right)_c = N e^{-E/T} \sum_i \frac{(2J_i + 1)\Gamma_i/2\pi \Gamma_{c,i}}{(E - E_i)^2 + \frac{1}{4}\Gamma_i^2 \Gamma_i}, \quad (10)$$

where $\Gamma_{c,i}/\Gamma_i$ denotes the branching ratio for the decay into channel c . Equations (9) and (10) describe the *primary* populations of states. In the present approximation, the relative populations of states depend only on the emission temperature of the system. However, the primary distributions can differ from the final populations of states which are detected experimentally due to feeding from higher-lying particle unstable states^{16,18,41,42}).

Historically, the sensitivity of two-particle correlation functions to the space-time extent of the emitting system was derived from the modifications of the wave functions of relative motion due to final-state interactions²⁷⁻³⁰) or quantum statistics²¹⁻²⁶). [For broad states decaying into particles of different charge to mass ratios or for nonresonant final state interactions between particles of different charge to mass ratios, Coulomb interactions with the heavy target residue lead to additional modifications of the correlation functions^{37,43}). For the case of narrow resonances, Coulomb interactions with the heavy target residue should be negligible.] If the time dependence of the emission process is neglected, one can express the two-particle correlation function in terms of the single-particle source function, $\rho(\mathbf{r})$, and the two-body wave function $\Psi(\mathbf{r}_1, \mathbf{r}_2)$:

$$R(q) = \int d^3r_1 d^3r_2 \{|\Psi(\mathbf{r}_1, \mathbf{r}_2)|^2 - 1\} \rho(\mathbf{r}_1) \rho(\mathbf{r}_2) \times \left(\int d^3r \rho(\mathbf{r}) \right)^{-2}. \quad (11)$$

By replacing the two-body wave function by its asymptotic form, assuming a uniform source function, and neglecting edge effects arising from the finite size of the reaction volume, one can recast³⁰) eq. (11) into the form of eq. (6). In this approximation, the thermal model is equivalent to the final state interaction model. For our calculations of the correlation functions, we have adopted the original formulation of Koonin, eq. (11), and assumed a source of gaussian spatial density, $\rho(\mathbf{r}) \propto \exp(-r^2/r_0^2)$, and negligible lifetime.

5. Two-particle inclusive measurements

5.1. CORRELATION FUNCTIONS

Inclusive two-particle correlation functions measured for the $^{14}\text{N} + ^{197}\text{Au}$ reaction at $E/A = 35$ MeV have already been published elsewhere^{19,35,37}). We will, therefore, only summarize the results.

Correlation functions measured at $\theta_{av} = 35^\circ$ and 50° are very similar in magnitude. This is illustrated in fig. 4 which shows the pp, p α , and d α correlation functions

measured at these angles. Apart from the energy thresholds no other constraints were applied. The pp correlation function²⁷⁾ exhibits a maximum near $q \approx 20$ MeV/c which is caused by the attractive singlet S-wave interaction between the detected protons. The p α correlation function⁴³⁾ is dominated by the p α resonance corresponding to the ground state of ${}^5\text{Li}$ ($J^\pi = \frac{3}{2}^-$, $\Gamma \approx 1.5$ MeV, $\Gamma_p/\Gamma = 1.00$); its line shape is distorted by the Coulomb interaction with the heavy target residue⁴³⁾. The rise of the correlation function towards small relative momenta, $q \leq 25$ MeV/c, is caused⁴³⁾ by contributions from the decay ${}^9\text{B} \rightarrow 2\alpha + p$. The d α correlation function^{16,19,29)} exhibits two maxima which correspond to the $T=0$ states in ${}^6\text{Li}$ at 2.186 MeV ($J^\pi = 3^+$, $\Gamma = 24$ keV, $\Gamma_\alpha/\Gamma_{\text{tot}} = 1.00$), 4.31 MeV ($J^\pi = 2^+$, $\Gamma = 1.3$ MeV, $\Gamma_\alpha/\Gamma_{\text{tot}} = 0.97$), and 5.65 MeV ($J^\pi = 1^+$, $\Gamma = 1.9$ MeV, $\Gamma_\alpha/\Gamma_{\text{tot}} = 0.74$).

The curves in fig. 4 represent two-particle correlation functions predicted in terms of the final state interaction model^{19,27,29,43)}, eq. (11). Because of the narrow width of the 2.186 MeV state in ${}^6\text{Li}$, the theoretical α d correlation function was corrected for the finite resolution of the hodoscope by folding the original calculation with a gaussian of appropriate width. Such corrections are of minor importance for the pp and p α correlation functions. (Since the height of the α d correlation function depends on the instrumental line shape, we have extracted source radii from the integral α d correlation, $R_{\text{eff}} = \int dq \cdot R(q)$, with the integration performed over the range of $q \approx 30$ –60 MeV/c. Source radii extracted in terms of this quantity are less dependent on the experimental resolution.) The inclusion of the temporal evolution of the emitting system is expected to reduce the magnitude of the calculated two-particle correlation functions^{27,29,44)}. Therefore, the indicated source dimensions represent upper limits for the spatial extent of the emitting system. The extracted upper limits of the source dimensions are comparable to, or slightly smaller than the size of the target nucleus [$r_0(\text{Au}) = \sqrt{\frac{2}{3}} r_{\text{rms}}(\text{Au}) \approx 4.3$ fm]. Source radii extracted from the broad peak of the α d correlation function at $q \approx 85$ MeV/c are larger by about 0.8 fm than those extracted from the sharp peak at $q \approx 40$ MeV/c; the reason for this discrepancy is not understood.

Inclusive two-particle correlation functions have been shown to depend on the total kinetic energy of the two coincident light particles^{18,19,32,35)}, possibly indicating emission from expanding or cooling (sub)systems. Fig. 5 summarizes the source parameters, r_0 , extracted³⁵⁾ from the inclusive two-particle correlation functions at $\theta_{\text{av}} = 35^\circ$. For orientation, the dashed horizontal lines mark the corresponding source dimensions of projectile and target nuclei. The extracted source parameters depend on the particle combination as well as on the total kinetic energy, $E_1 + E_2$, of the two coincident particles³⁵⁾. These dependences are not yet understood quantitatively.

5.2. YIELDS OF PARTICLE UNSTABLE ${}^6\text{Li}$ NUCLEI

The α d correlation functions shown in fig. 4 are dominated by $T=0$ states in ${}^6\text{Li}$. Following ref. ¹⁶⁾, we assume that the coincidence yield, Y_c , resulting from the

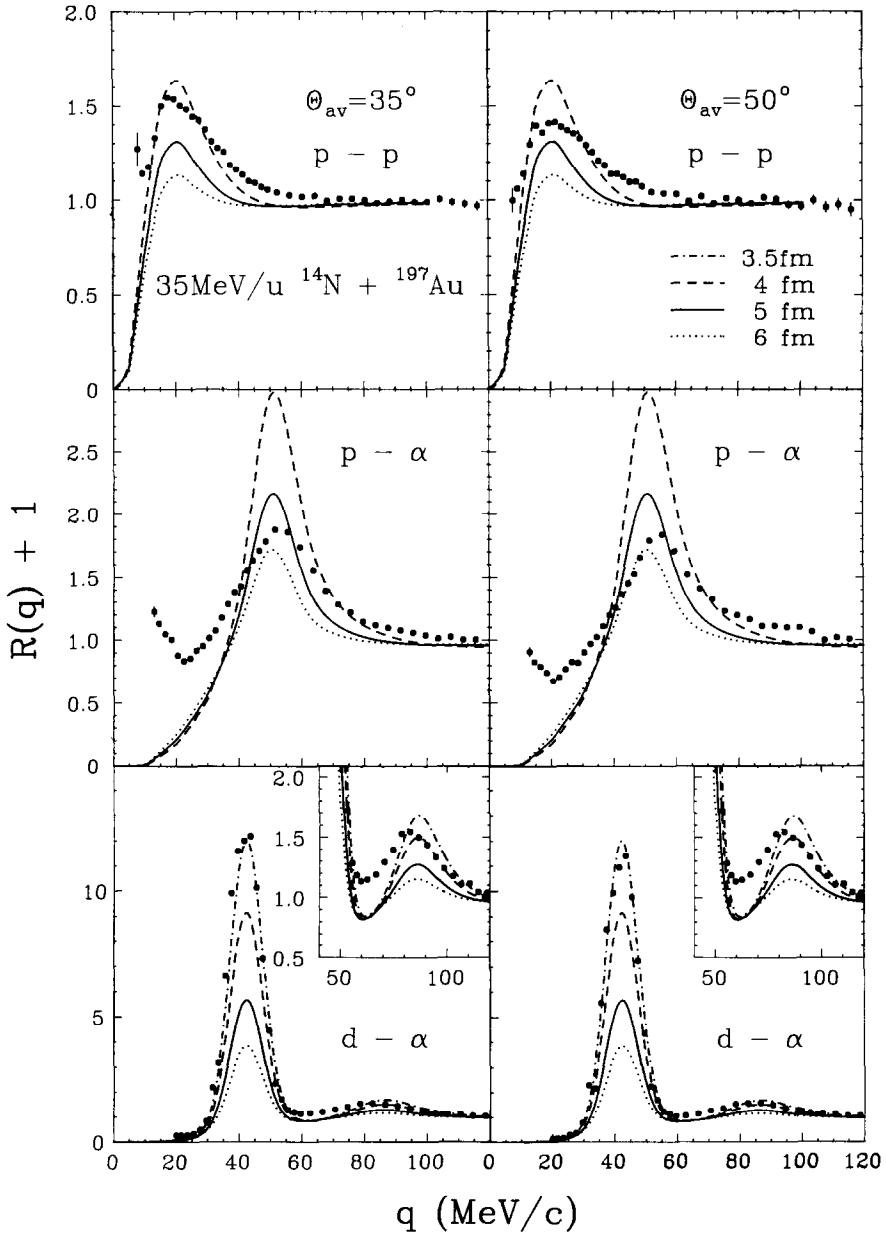


Fig. 4. Inclusive pp , $p\alpha$, and $d\alpha$ correlation functions measured at $\theta_{av}=35^\circ$ and 50° . Apart from the energy thresholds, no constraints were applied to generate the experimental correlation functions. The theoretical correlation functions were calculated with the final-state interaction model^{27,29}, eq. (11).

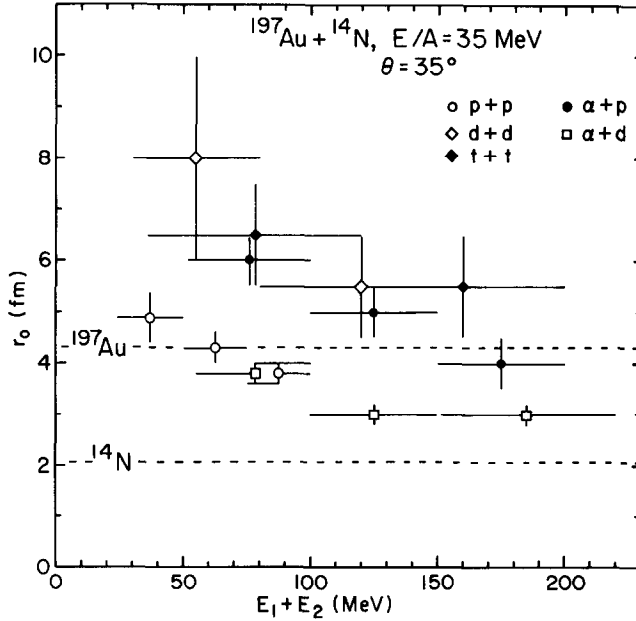


Fig. 5. Source parameters extracted³⁵⁾ from inclusive two-particle correlation functions measured at $\theta_{av} = 35^\circ$. The dashed lines indicate the corresponding dimensions of projectile and target; $E_1 + E_2$ denotes the total kinetic energy of the detected particles.

decay of particle unstable states is given by:

$$Y_c(\mathbf{p}_1, \mathbf{p}_2) = Y_{12}(\mathbf{p}_1, \mathbf{p}_2) - C_{12} Y_1(\mathbf{p}_1) Y_2(\mathbf{p}_2) (1 + R_b(q)), \quad (12)$$

where $R_b(q)$ denotes the background correlation function and C_{12} is the normalization constant defined in eq. (2). We have used the same background correlation function as in refs.^{16,19)} to extract the αd coincidence yields resulting from the decay of particle unstable ${}^6\text{Li}$ nuclei. Fig. 6 shows the extracted yields as a function of the relative kinetic energy, $T_{c.m.}$, in the ${}^6\text{Li}$ rest frame; only statistical errors are shown.

The experimental yield, Y_c , is related to the excitation energy spectrum decaying into channel c , $(dn(E)/dE)_c$, by the relation

$$Y_c(E') = \int dE \varepsilon_c(E', E) \left(\frac{dn(E)}{dE} \right)_c. \quad (13)$$

Here, $\varepsilon_c(E', E)$, is the efficiency function of the hodoscope; E and E' are the actual and measured excitation energies, respectively. (The excitation energy, E , and the relative kinetic energy, $T_{c.m.}$, are related to the separation energy, Q_s , via: $E = T_{c.m.} + Q_s$.) The efficiency functions for our hodoscope were determined by Monte Carlo calculations which take into account the geometry of the hodoscope, the detector energy resolutions, and the constraints on the particle energies. The decays of the

parent nuclei were assumed to be isotropic in their center-of-mass frames. The laboratory energy spectra and angular distributions of the ${}^6\text{Li}$ parent nuclei were described in terms of eq. (1) with the parameters given in table 1; these distributions are shown by the solid lines in fig. 2.

The dot-dashed, dashed, solid, and dotted curves in fig. 6 show the coincidence yields predicted in terms of eq. (13) assuming thermal distributions, eq. (10), with $T = 1, 2.5, 5,$ and 10 MeV, respectively. The curves are normalized to reproduce the experimental yield integrated over the energy range of $T_{\text{c.m.}} = 0.3\text{--}1.2$ MeV. By integrating the decay yields over the energy ranges of $T_{\text{c.m.}} = 0.25\text{--}1.45$ and $1.5\text{--}6.25$ MeV and comparing the ratio of these yields to the corresponding ratio calculated from eqs. (10) and (13), an average emission temperature of $T \approx 4$ MeV is extracted¹⁹⁾. This value is believed to be accurate to within about 25% due to uncertainties in the αd background correlation function and due to the saturation of the coincidence yields at higher temperatures; statistical uncertainties are negligible¹⁹⁾. However, additional uncertainties result from the unknown magnitude of feeding from higher-lying states^{41,42)}.

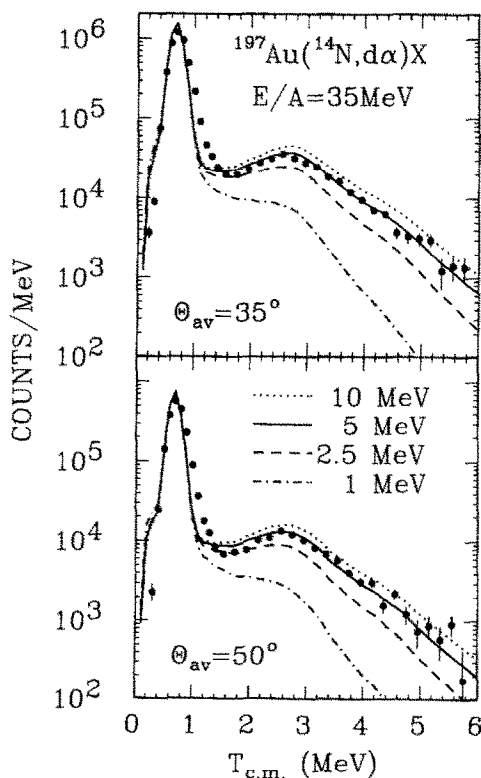


Fig. 6. Energy spectrum resulting from the decay of particle-unstable states in ${}^6\text{Li}$. The curves correspond to thermal distributions with $T = 1, 2.5, 5,$ and 10 MeV, taking the response of the hodoscope into account.

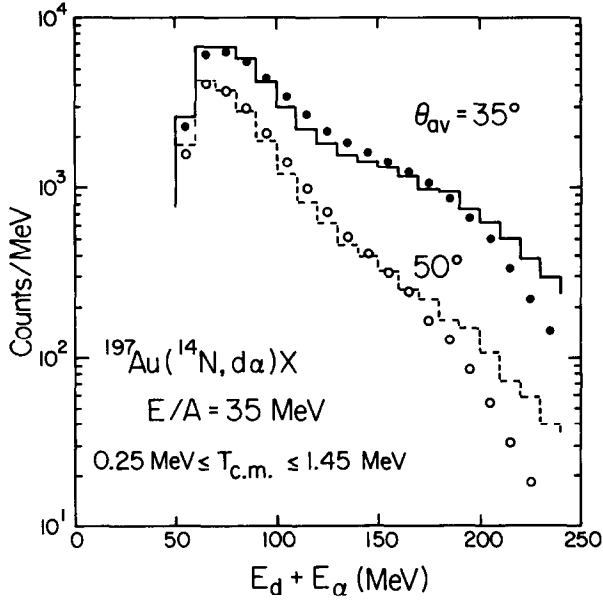


Fig. 7. Measured αd coincidence yield resulting from the decay ${}^6\text{Li}_{2,186}^* \rightarrow \alpha + d$ as a function of the total kinetic energy, $E_\alpha + E_d$. The histogram is the result of the Monte Carlo calculations described in the text.

To test the assumptions of our Monte Carlo calculations, we examined the decay of ${}^6\text{Li}_{2,186}^* \rightarrow \alpha + d$. Fig. 7 shows the total kinetic energy distribution, $dY_c/d(E_\alpha + E_d)$, integrated over the first peak in the ${}^6\text{Li}$ excitation energy spectrum, $T_{c.m.} = 0.3\text{--}1.2$ MeV. The yields predicted by the Monte Carlo calculations are shown by the solid histograms. The data are consistent with our assumptions about the parent energy distribution.

Angular distributions, $dY_c/d\theta_R$ and $dY_c/d\Phi_R$, of the decay yields from the 2.186 MeV state in ${}^6\text{Li}$ are shown in fig. 8. Here, θ_R is defined by: $\cos(\theta_R) = (\mathbf{P} \cdot \mathbf{q}) / (|\mathbf{P}| \cdot |\mathbf{q}|)$, where $\mathbf{P} = \mathbf{p}_1 + \mathbf{p}_2$ is the total momentum; Φ_R is defined by: $\cos(\Phi_R) = ((\mathbf{n}_b \times \mathbf{P}) \cdot \mathbf{q}) / (|\mathbf{n}_b \times \mathbf{P}| \cdot |\mathbf{q}|)$, where \mathbf{n}_b is a unit vector parallel to the beam direction. The histogram shows the result of our Monte Carlo calculations. (The asymmetry of $dY_c/d\Phi_R$ with respect to $\Phi_R = 90^\circ$ is caused by the binning during the analysis of the experimental and simulated data.) It was verified that details of the θ_R distribution are sensitive to uncertainties in the absolute energy calibration. Within these uncertainties, the data are consistent with the assumption of isotropic decay.

6. Filtered single-particle distributions

Folding angle distributions between two fission fragments measured in coincidence with protons, deuterons, tritons, α -particles and Li nuclei, detected at $\theta_{av} = 20^\circ$, are shown in fig. 9. For orientation, the upper scale gives an approximate scale for the

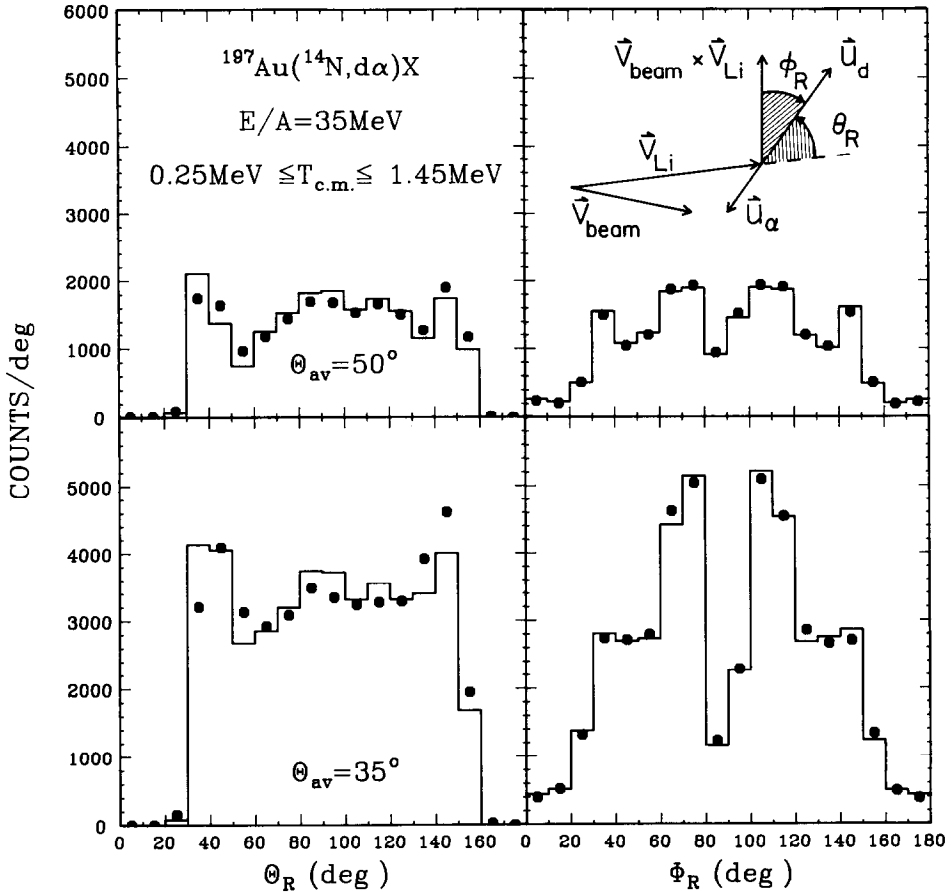


Fig. 8. Angular distributions of the decay yields from the decay ${}^6\text{Li}_{2,186}^* \rightarrow \alpha + d$. The angles θ_R and ϕ_R are defined in the text and depicted in the insert. The histograms are the results of Monte Carlo calculations in which the ${}^6\text{Li}$ nuclei are assumed to decay isotropically in their respective rest frames.

fraction, $\Delta p/p$, of the projectile momentum which is transferred to the heavy reaction residue. This scale gives the relation between the linear momentum of the fissioning system and the most probable folding angle between two fission fragments resulting from the symmetric fission of the composite nucleus. With increasing mass of the detected light particle, the maximum of the coincident folding angle distribution is shifted towards larger angles. To a large extent, this effect is due to momentum conservation: Heavier particles emitted at forward angles carry away a larger fraction of the projectile momentum.

Even for the ideal case of fission of a composite nucleus with unique spin, excitation energy, and recoil momentum, rather broad folding angle distributions will be measured because of the finite widths of the mass and kinetic energy

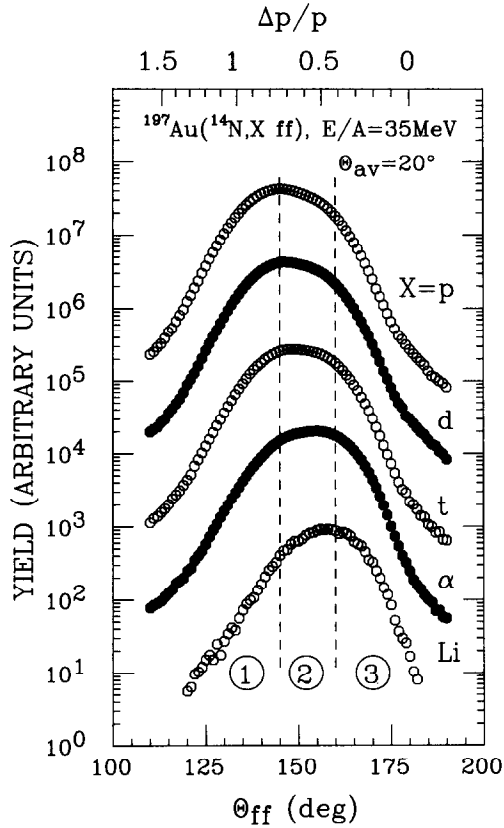


Fig. 9. Folding angle distributions between two coincident fission fragments detected in coincidence with p, d, t, α , and Li nuclei emitted at $\theta_{av}=20^\circ$. The dashed lines depict the boundaries of the folding angle gates (1), (2), and (3).

distributions of the fission fragments and because of additional broadening by light-particle evaporation. For this reason, gates on folding angle distributions do not select a sharply defined range of recoil momenta. Instead, they correspond to a filter of moderate resolution which, nevertheless, can serve to enhance or suppress reactions associated with small or large linear momentum transfers.

In order to discriminate between reactions associated with small or large linear momentum transfers to the heavy reaction residue, we define three different gates on folding angle. The boundaries of these gates are indicated by the dashed vertical lines in fig. 9. More specifically, these gates are defined by: $\theta_{ff} < 145^\circ$ (gate 1), $145^\circ \leq \theta_{ff} \leq 160^\circ$ (gate 2), and $\theta_{ff} > 160^\circ$ (gate 3). Because of the low fissility of nuclei with $Z \approx 80$, target residues with excitation energies of less than a few tens of MeV will not fission; the study of such gentle collisions necessitates the use of more fissile, heavier target nuclei such as uranium, see e.g. refs. ^{45,46}). Nevertheless, we

will use the term “peripheral, quasi-elastic collisions” for reactions filtered by large folding angles ($\theta_{ff} > 160^\circ$, gate 3). It should then be clear, that this operational definition excludes the most gentle of these collisions.

The effects of filtering light-particle energy spectra by the three folding angle gates are illustrated in figs. 10–12. The spectra were obtained by summing the corresponding yields over all detectors of the hodoscope with the center of the hodoscope placed at $\theta_{av} = 20^\circ$. The absolute normalization of the vertical scale is in arbitrary units; relative normalizations are proportional to the ratio N_{ff}^c/N_{ff} , where N_{ff}^c corresponds to the number of triple coincidences (light particle+two fission fragments) and N_{ff} corresponds to the number of two-fold coincidences (two fission fragments) for a given constraint on folding angle. Figs. 10 and 11 show the spectra of hydrogen and helium isotopes, respectively. The right-hand part of fig. 12 shows the spectrum of particle stable Li nuclei. The left-hand part of the figure shows the dependence of the measured αd coincidence yield on the total kinetic energy, $E_\alpha + E_d$, for αd pairs which can be attributed to the 2.186 MeV state in ${}^6\text{Li}$. (This yield was obtained by placing a gate on the relative kinetic energy of the two coincident particles, $E_{rel} = q^2/2\mu = 0.3\text{--}1.2$ MeV, and subtracting the “background” coincidence yield, see also eq. (12).) The yields shown in the center part of the figure were corrected for the energy dependence of the hodoscope efficiency. Energy spectra gated by large folding angles, i.e. by small linear momentum transfers (gate 3, $\theta_{ff} > 160^\circ$), exhibit pronounced quasi-elastic components centered close to the

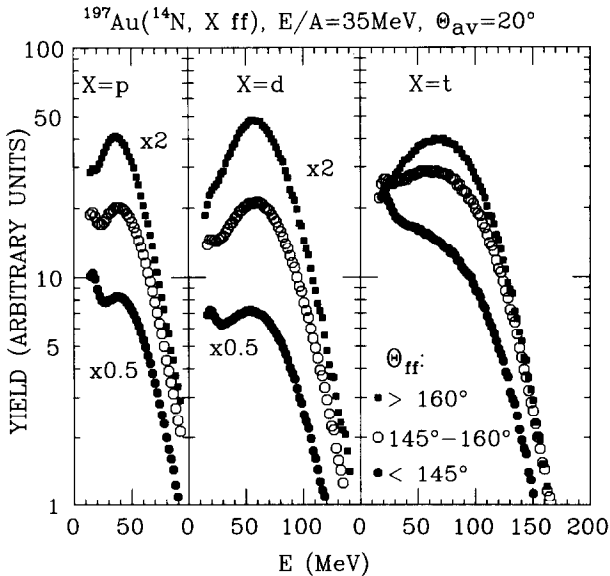


Fig. 10. Yields of protons, deuterons and tritons summed over all elements of the hodoscope with the center of the hodoscope positioned at $\theta_{av} = 20^\circ$. The distributions are shown for the three gates on folding angle defined in fig. 9.

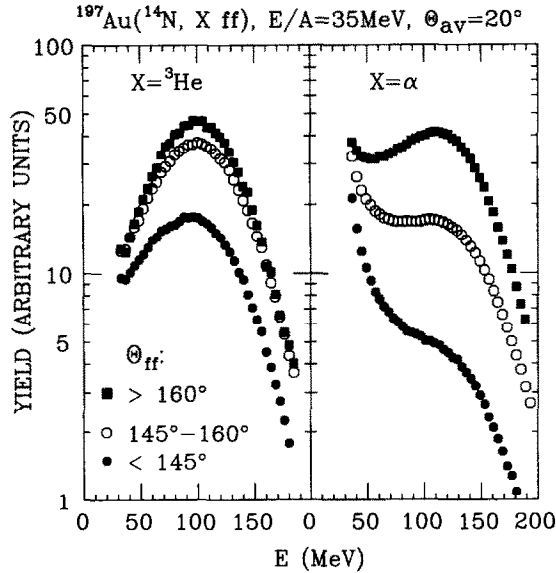


Fig. 11. Yields of ${}^3\text{He}$ and ${}^4\text{He}$ nuclei summed over all elements of the hodoscope with the center of the hodoscope positioned at $\theta_{\text{av}} = 20^\circ$. The distributions are shown for the three gates on folding angle defined in fig. 9.

projectile velocity. These components are strongly suppressed by gating on small folding angles, i.e. large linear momentum transfers (gate 1, $\theta_{\text{ff}} < 145^\circ$).

These observations support the intuitive picture which associates large folding angles with collisions at large impact parameters for which break-up reactions or sequential decays of excited projectile residues are important. Smaller folding angles, on the other hand, are associated with less peripheral and more violent collisions in which a major part of the projectile momentum is absorbed by the heavy target nucleus. In general, gate 1 serves as an effective filter condition to suppress the quasi-elastic, beam velocity components in the energy spectra. Since beam velocity particles can also be emitted in absorptive breakup or massive transfer reactions characterized by large momentum transfers to the heavy reaction residue, the suppression of the beam velocity component is not perfect. In fact, small residual beam velocity components can be discerned in most of the gated energy spectra. It is remarkable that the ${}^3\text{He}$ energy spectra are dominated by the beam velocity component irrespective of the gating condition, see fig. 11. Possibly, ${}^3\text{He}$ nuclei are preferentially produced in more direct reactions and only to a lesser extent in statistical emission processes.

Fig. 13 shows the differential yields, $d^2Y(E, \theta)/dE d\Omega$, of α -particles and lithium nuclei emitted at forward angles and gated by the three constraints on folding angle. In order to be able to make reasonable assumptions about the distributions of particle unstable ${}^5\text{Li}$ and ${}^6\text{Li}$ nuclei (see sects. 7.2 and 7.3) we have fit these yields

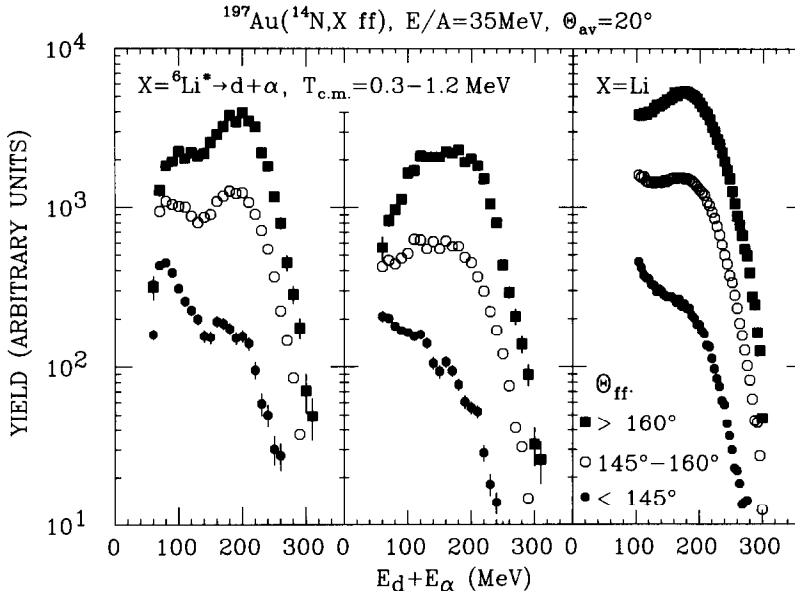


Fig. 12. Left-hand part: Dependence of the αd coincidence yield on the total kinetic energy, $E_\alpha + E_d$, for αd pairs which can be attributed to the decay of the 2.816 MeV state in ${}^6\text{Li}$. Center part: Same as left-hand part, but corrected for the variation of the hodoscope efficiency with $E_\alpha + E_d$. Right-hand part: Yields of lithium nuclei summed over all elements of the hodoscope. The distributions are shown for the three gates on folding angle defined in fig. 9. The center of the hodoscope was positioned at $\theta_{av} = 20^\circ$.

with the parametrization of eq. (1). The fits are shown by the solid lines in fig. 13; the parameters are listed in table 2.

7. Filtered two-particle distributions

7.1. αd CORRELATION FUNCTIONS

Fig. 14 shows αd correlation functions measured in coincidence with two fission fragments. For these measurements, the center of the hodoscope was placed at $\theta_{av} = 20^\circ$. For each of the three gates on folding angle, the correlation functions are shown for two different constraints on the total kinetic energy, $E_d + E_\alpha$, of the two coincident light particles. The curves represent theoretical correlation functions predicted by the final-state interaction model, eq. (11).

Fig. 15 summarizes the dependence of αd correlations on the total energy per nucleon, $(E/A)_{tot} = \frac{1}{6}(E_\alpha + E_d)$, of the two coincident particles. Inclusive correlations and correlations measured in coincidence with fission fragments are shown in the right- and left-hand parts of the figure, respectively. The left-hand scale of the figure gives the integral correlation, $R_{eff} = \int dq \cdot R(q)$, integrated over the range of $q = 30\text{--}60$ MeV/c; the right-hand scale of the figure gives the extracted source radii, r_0 .

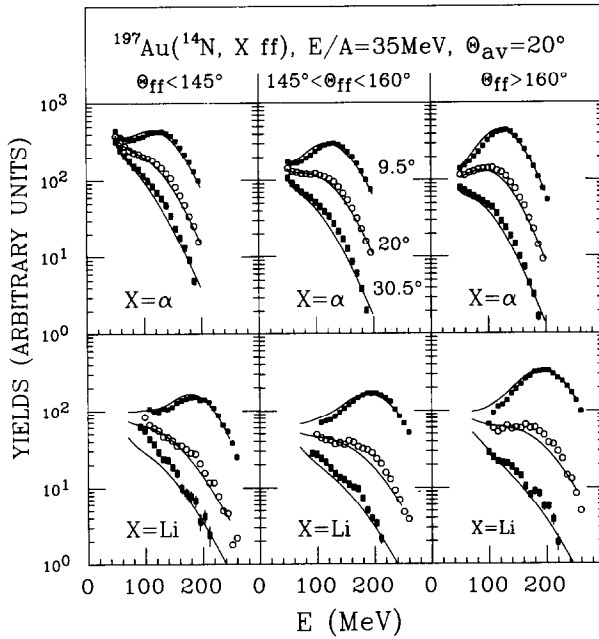


Fig. 13. Differential yields, $d^2Y(E, \theta)/dE d\Omega$, of α -particles and lithium nuclei emitted at forward angles and gated by the three folding angle gates. The solid lines show fits with the parametrization of eq. (1). The parameters are listed in table 2.

TABLE 2
Parameters used to fit the gated yields shown in fig. 13

Particle (gate #)	U_c (MeV)	T_1 (MeV)	v_1/c	N_1 (a.u.)	T_2 (MeV)	v_2/c	N_2 (a.u.)	T_3 (MeV)	v_3/c	N_3 (a.u.)
α (1)	16.1	8.0	0.002	346.6	16.7	0.118	43.26	6.1	0.233	8.553
α (2)	16.1	8.0	0.017	265.0	13.8	0.150	66.06	6.1	0.236	29.99
α (3)	16.1	8.0	0.000	146.0	11.8	0.168	23.70	5.0	0.236	14.79
Li (1)	16.1	9.8	0.040	37.5	13.9	0.149	18.57	3.6	0.220	6.62
Li (2)	16.1	13.4	0.054	10.8	13.2	0.166	6.16	4.7	0.227	3.87
Li (3)	16.1	14.9	0.071	62.2	11.2	0.187	33.23	4.2	0.228	27.7

At low energies, the αd correlations are of comparable magnitude. For small linear momentum transfers (gate 3), they are nearly independent of energy. For larger linear momentum transfers, on the other hand, the αd correlations vary strongly with energy. For the inclusive correlations, right-hand part of fig. 15, a similar energy dependence exists^{19,35}). It becomes more pronounced at larger angles, θ_{av} , where contributions from quasi-elastic processes become less important.

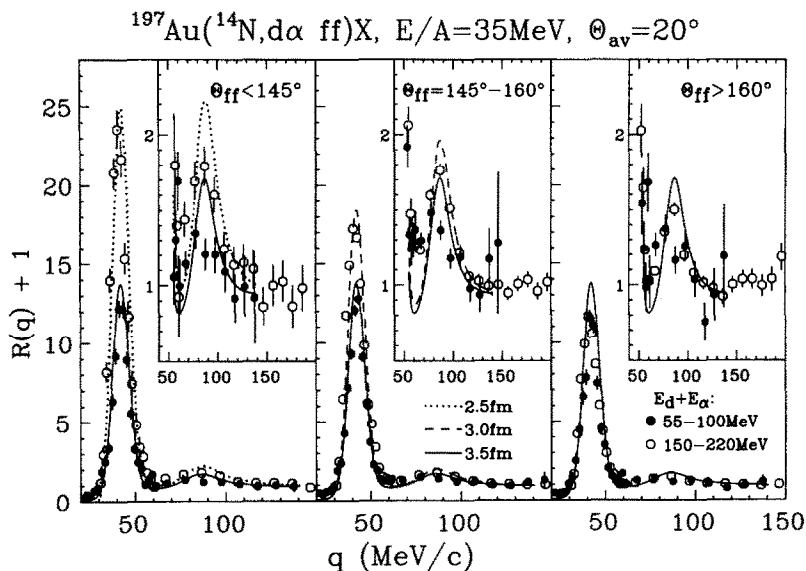


Fig. 14. $d\alpha$ correlation function measured at $\theta_{\text{av}}=20^\circ$ in coincidence with two fission fragments. The constraints placed on θ_{ff} and on $E_\alpha + E_d$ are indicated in the figure. The theoretical correlation functions were calculated with the final state interaction model²⁹⁾, eq. (11).

The extracted source sizes are generally smaller than the size of the target nucleus ($r_0(\text{Au}) = \sqrt{2/3} r_{\text{rms}}(\text{Au}) \approx 4.4$ fm). A strictly geometric interpretation of the extracted radius parameters would imply that peripheral collisions are characterized by sources significantly larger than the size of the projectile nucleus ($r_0(\text{N}) \approx 2.1$ fm). For this class of reactions emission from the projectile must be important as evidenced by the strong quasi-elastic component of the energy spectra. Source radii larger than the radius of the projectile are unlikely to reflect the true geometric source dimensions. Therefore, temporal effects cannot be neglected when interpreting the present correlation functions.

The time scales characteristic of preequilibrium particle emission in violent fusion-like collisions may be shorter than those which characterize particle emission in quasi-elastic reactions thus producing stronger correlations and smaller apparent source radii. Our observation of reduced correlations for peripheral processes may, therefore, reflect longer emission time scales rather than larger source dimensions. The sequential decay of excited projectile residues is an example for reactions which proceed via longer emission time scales. For such processes, Koonin's formulation may be less useful for the calculation of two-particle correlation functions and alternative statistical formulations, such as appropriate generalizations of the Hauser-Feshbach theory, could be explored. For the case of equilibrium decay of light compound nuclei, Hauser Feshbach calculations have predicted⁴⁷⁾ smaller two-proton correlations than expected from the zero-lifetime limit of Koonin's

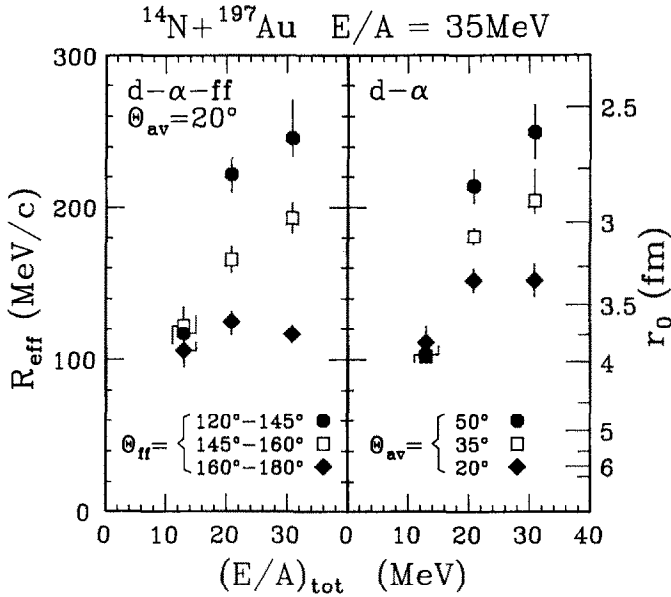


Fig. 15. Dependence of αd correlations on the total energy per nucleon, $(E/A)_{\text{tot}} = \frac{1}{2}(E_{\alpha} + E_d)$, of the two coincident particles. Correlations measured inclusively and in coincidence with fission fragments are shown in the right- and left-hand parts, respectively. The left-hand scale corresponds to $R_{\text{eff}} = \int dq \cdot R(q)$, with the integration performed over the range of $q = 30\text{--}60$ MeV. The right-hand scale gives source radii extracted with the final-state interaction model²⁹, eq. (11). [Data for $\theta_{\text{av}} = 35^{\circ}$ and 50° were taken from ref. 19].]

model. Within Koonin's model, one expects reduced correlations for peripheral collisions if contributions from the decay of equilibrated projectile residues are important. For fusion-like collisions, on the other hand, such processes are suppressed when the energy of the detected particles is sufficiently high to exclude evaporation from the equilibrated heavy reaction residue. Reduced correlations for particles of lower energies, emitted in fusion-like reactions, could then be interpreted in terms of sequential particle evaporation from the equilibrated heavy reaction residue. Indeed, recent numerical simulations for the statistical decay of a highly excited, equilibrated nucleus⁴⁴) suggest that the observed energy dependence of two-particle correlation functions could be caused by the fact that more energetic particles are emitted at higher temperatures and at shorter time intervals than particles of lower energy which are emitted at larger time intervals.

The statistics collected in the present experiment were insufficient to explore the simultaneous dependence of the pp and $p\alpha$ correlation functions on linear momentum transfer and outgoing particle energy. These correlation functions, too, exhibit more pronounced peaks when gated on small folding angles; however, the effect appears to be less dramatic than for the αd correlation function [see ref. 36) and fig. 18, next section].

7.2. DECAY OF PARTICLE UNSTABLE ${}^6\text{Li}$ NUCLEI

Since fission fragments are preferentially emitted in the entrance channel scattering plane⁴⁸⁾ the assumption of isotropic decay of particle unstable states can be addressed more sensitively for the decays measured in coincidence with fission fragments. By gating on different ranges of folding angles one may also explore whether the assumption of isotropic decay is only violated for specific classes of reactions. This information is important for the extraction of the relative populations of states. It can be evaluated for the decay of the sharp 2.186 MeV state in ${}^6\text{Li}$. For this state, uncertainties due to the subtraction of the uncorrelated background are minimal.

Fig. 16 shows the dependence of the αd coincidence yield from the decay of ${}^6\text{Li}_{2.816} \rightarrow \alpha + d$ as a function of the angles θ_R and Φ_R already defined in sect. 5.2, see also fig. 8. These yields were gated by the three constraints on folding angle defined in fig. 9. The histograms show the results of Monte Carlo calculations based on the assumption of isotropic decay in the rest frame of the parent nucleus. In these calculations, the differential cross sections for the emission of the primary ${}^6\text{Li}_{2.186}$ nuclei were extrapolated in terms of the moving source parameterization, eq. (1), using the parameters given in table 2. The calculations are in good agreement

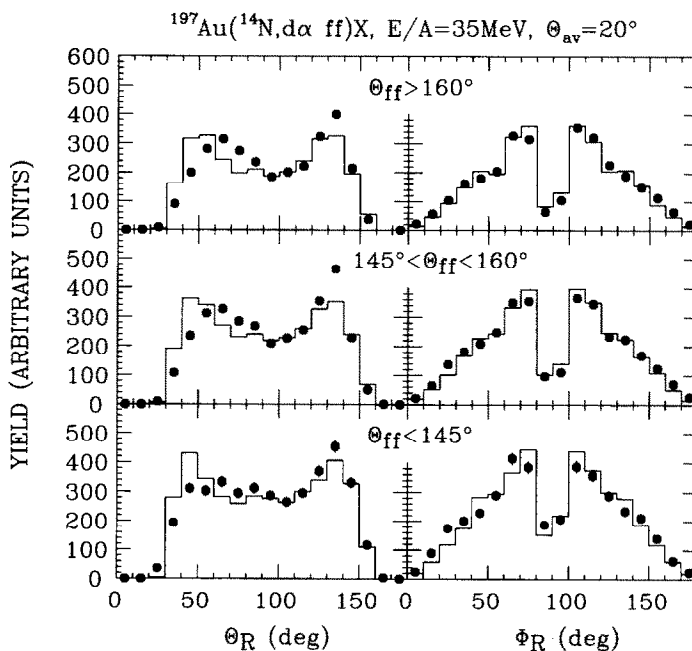


Fig. 16. Angular distributions of the αd yields resulting from the decay ${}^6\text{Li}_{2.186}^* \rightarrow \alpha + d$, gated on the three different gates on folding angle defined in fig. 9. The angles θ_R and Φ_R were defined in sect. 5.2 (see also fig. 8). The histograms show the results of Monte Carlo calculations in which the ${}^6\text{Li}$ nuclei are assumed to decay isotropically in their respective rest frames.

with the data; remaining small discrepancies can be attributed to uncertainties of the energy calibrations. No evidence can be established for significant violations of the assumption of isotropic decay.

In order to extract emission temperatures, we determined the ${}^6\text{Li}^* \rightarrow \alpha + d$ coincidence yields, N_L and N_H , integrated over the energy ranges of $T_{c.m.} = 0.3 - 1.45$ and $1.5 - 6.25$ MeV, respectively. The shaded horizontal bands in fig. 17 show the yield ratios, N_L/N_H , extracted for events selected by the three folding angle gates defined in fig. 9. The additional constraint, $E_\alpha + E_d \geq 100$ MeV, was applied to reduce contributions from the decay of equilibrated target nuclei. The widths of the shaded bands reflect uncertainties of the background subtraction caused by limited coincidence statistics at large relative momenta. The solid lines show the temperature dependence of the coincidence yield ratios predicted for thermal distributions, see eqs. (10) and (13). (For these calculations, the distributions of particle unstable ${}^6\text{Li}$ nuclei were parametrized in terms of eq. (1); the parameters are listed in table 2. In fig. 13, these distributions are compared to the measured Li yields.) The shaded vertical bands in fig. 17 indicate the range of temperatures consistent with the

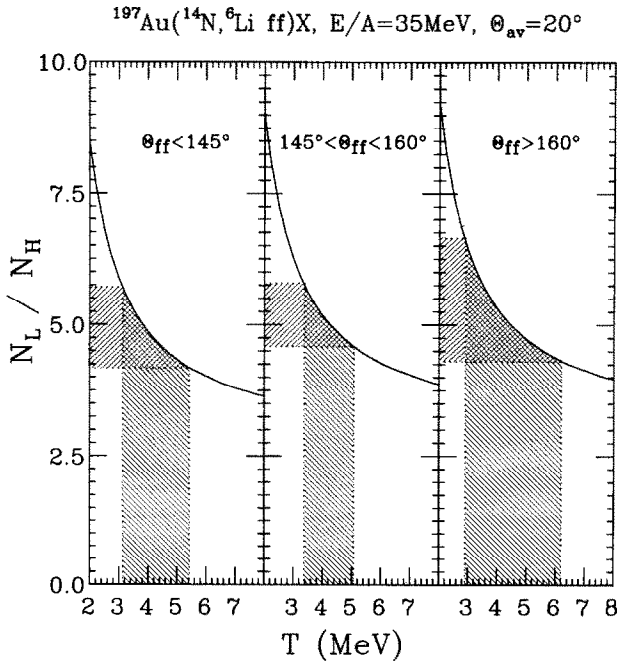


Fig. 17. Ratios, N_L/N_H , of measured αd coincidence yields resulting from the decays of particle unstable ${}^6\text{Li}$ nuclei. The yields N_L and N_H were integrated over the energy ranges of $T_{c.m.} = 0.3 - 1.45$ and $1.5 - 6.25$ MeV, respectively. Gates on folding angle are given in the figure. The hatched regions indicate the experimental values. The solid curves show the temperature dependences of yields predicted by eqs. (10) and (13).

experimental yield ratios; typical values are of the order of 4 MeV. These temperatures have considerable uncertainties due to the small energy separation of the states considered. Additional systematic errors could be caused by sequential feeding from higher-lying particle unstable states ^{41,42}).

7.3. DECAY OF PARTICLE UNSTABLE ⁵Li NUCLEI

More accurate temperature determinations could be made from the relative populations of the ⁵Li ground state, ⁵Li_{gs} → α + p, and the 16.7 MeV state, ⁵Li_{16.7} → d + ³He. Statistical calculations indicate ^{41,42}) negligible feeding of these two states from the decay of known particle unstable states if the emission temperatures are smaller than about 8 MeV. Since these two states are separated by a large energy interval, their relative populations depend strongly on excitation energy. Unfortunately, our detector geometry had not been optimized for the detection of the decay of the 16.7 MeV state in ⁵Li which lies close to the d + ³He threshold. Because of the relatively large angular separation between adjacent detectors, Δθ = 6.1°, the thresholds on the total kinetic energy were lowered to E_d + E_{³He} = E_p + E_α = 52 MeV. The dependence of the extracted emission temperatures on the total kinetic energy could not be explored.

Figs. 18 and 19 show the αp and d³He correlations functions, respectively, gated by the three constraints on folding angles defined in fig. 9. The broad peak in the

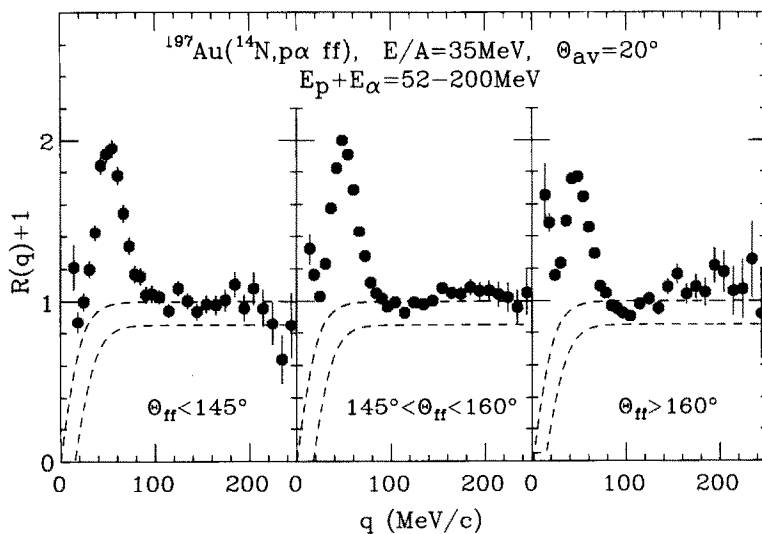


Fig. 18. pα correlation functions measured in coincidence with two fission fragments. The gates on folding angle are given in the figure. The dashed lines indicate the bounds within which the background correlation function was assumed to lie.

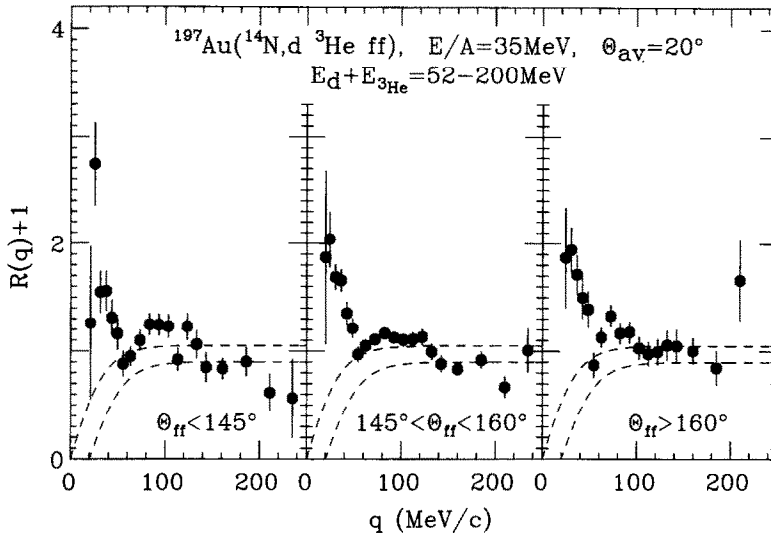


Fig. 19. $d^3\text{He}$ correlation functions measured in coincidence with two fission fragments. The gates on folding angle are given in the figure. The dashed lines indicate the bounds within which the background correlation function was assumed to lie.

αp correlation function at $q \approx 50 \text{ MeV}/c$ corresponds to the decay ${}^5\text{Li}_{\text{gs}} \rightarrow \alpha + p$; the maximum of the $d^3\text{He}$ correlation function at small relative momenta is due to the decay ${}^5\text{Li}_{16.7} \rightarrow d + {}^3\text{He}$. The coincidence yields, N_L and N_H , from the decays of the low-lying ground state and the high-lying 16.7 MeV state, respectively, were extracted according to eq. (12). The extreme limits within which the background correlation functions were assumed to vary are shown by the dashed curves in figs. 18 and 19. The extracted yield ratios, N_L/N_H , are shown by the shaded horizontal bands in fig. 20.

For measurements close to the grazing angle, the shapes of the energy spectra of particle stable nuclei change rapidly with detection angle, see fig. 13. In addition, they depend sensitively on the gate on folding angle, see figs. 10–12. Since stable ${}^5\text{Li}$ nuclei do not exist, the shapes of the energy and angular distributions of the emitted ${}^5\text{Li}$ parent nuclei are not known. We have assumed that the ${}^5\text{Li}$ parent distributions could be described in terms of a superposition of three maxwellian distributions, the parameters of which were taken from fits to the α -particle and Li cross sections shown in fig. 13. The extrapolated ${}^5\text{Li}$ distributions are shown by the solid and dashed curves in fig. 21. The solid curves represent distributions extrapolated by using source parameters extracted from fits to the α -particle yields; the dashed curves represent distributions predicted from fits to the Li yields. The differences between these two extrapolations illustrate the large uncertainties which have to be attributed to the ${}^5\text{Li}$ parent distributions. However, relative detection

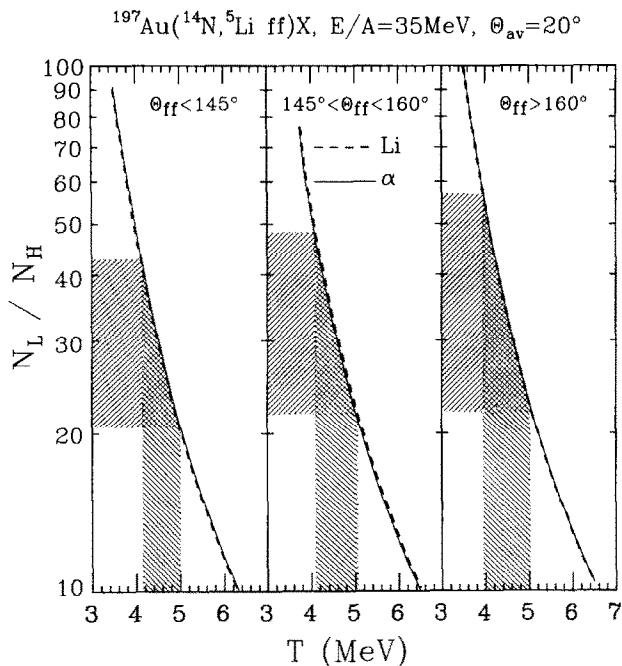


Fig. 20. Yield ratios N_L/N_H for the detection of the decays $^5\text{Li}_{\text{gs}} \rightarrow \alpha + p$ and $^5\text{Li}_{16,7} \rightarrow d + ^3\text{He}$ in coincidence with two fission fragments. The gates on folding angle are given in the figure. The hatched regions indicate the range of values consistent with our assumptions on the background correlation functions shown in figs. 18 and 19. The solid and dashed curves show the temperature dependences of yields predicted by eqs. (10) and (13) assuming parent distributions given by eq. (1) with parameters extracted from fits to the α -particle and Li distributions shown in fig. 13. The parameters are given in table 2.

efficiencies are rather insensitive to the detailed shape of the parent distributions. This is illustrated by the solid and dashed curves in fig. 20 which show the temperature dependence of thermal yields ratios (eqs. (10), (13)) predicted for the two sets of parent distributions. The two predicted yield ratios are nearly indistinguishable. It is, therefore, possible to extract emission temperatures from the relative populations of states in ^5Li in spite of large uncertainties concerning the shape of the parent distributions.

The shaded vertical bands in fig. 20 indicate the ranges of emission temperatures which are consistent with our assumptions on the background correlation functions. The temperatures extracted for the three gates on folding angles are of the order of 4–5 MeV. These values are consistent with those extracted from the decays of particle unstable ^6Li nuclei. The surprising similarity of emission temperatures extracted for peripheral and fusion-like collisions could be related to the fact that our fission filter suppresses the most gentle types of collisions. It was already stressed

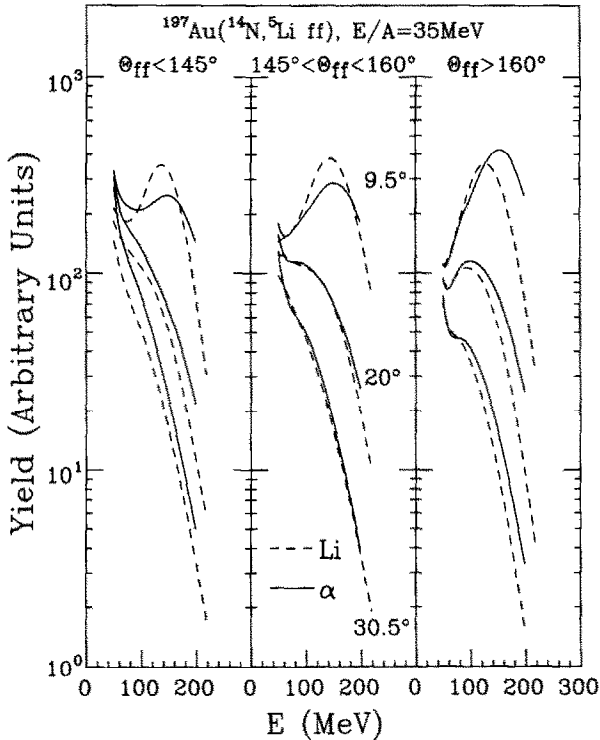


Fig. 21. ${}^5\text{Li}$ parent distributions assumed for the efficiency calculations shown by the solid and dashed lines in fig. 20.

before that the study of such gentle collisions requires the use of more fissile targets. Such measurements would clearly be useful.

8. Summary and conclusion

We have investigated single- and two-particle distributions of light nuclei emitted in ${}^{14}\text{N}$ induced reactions on ${}^{197}\text{Au}$ at $E/A = 35$ MeV. The single-particle inclusive distributions measured in this experiment can be described as a sum of three maxwellian distributions ("moving sources"). At forward angles, the cross sections are dominated by a fast source which could be associated with particle emission from projectile residues. At intermediate angles, the high energy portions of the energy spectra are dominated by an intermediate rapidity source which is generally associated with particle emission during the early nonequilibrated stages of the reaction. The temperature parameters which characterize the energy spectra of light particles emitted at intermediate rapidity follow the systematics established in

refs. ^{8,39}). The low energy portions of the energy spectra are dominated by a slow source which could be attributed to particle emission from the later more equilibrated stages of the reaction, e.g. particle evaporation from equilibrated heavy reaction residues.

Inclusive two-particle correlations at small relative momenta were measured at several average emission angles, $\theta_{av} = 20^\circ$, 35° , and 50° . More energetic particles were observed to exhibit more pronounced correlations. This energy dependence is not limited to particle emission close to the grazing angle as had been surmised previously ⁴⁹). It could indicate that particles of different energies originate (on the average) from different stages of the reaction characterized by different source dimensions or different (average) time intervals between subsequent emission processes.

Mean emission temperatures of $T \approx 4$ MeV were extracted from the relative populations of particle unbound $T = 0$ states in ${}^6\text{Li}$. The relative populations of these states were found to depend on the kinetic energy of the emitted ${}^6\text{Li}$ parent nuclei ¹⁹): Higher emission temperatures were extracted ¹⁹) for particles emitted with higher kinetic energies. Such an energy dependence was not observed ¹⁸) for ${}^{40}\text{Ar}$ induced reactions on ${}^{197}\text{Au}$ at $E/A = 60$ MeV. Because of the small energy separation of the $T = 0$ states in ${}^6\text{Li}$, their relative populations are not very sensitive to emission temperatures $T \geq 5$ MeV. Unfortunately, our detector geometry did not permit the exploration of the energy dependence of the populations of states in ${}^5\text{Li}$ which are more sensitive to the temperature of the emitting system and less sensitive to perturbations of the initial populations (such as sequential decay).

In order to investigate dependences on specific classes of reactions, single- and two-particle distributions were measured in coincidence with two fission fragments resulting from the decay of heavy reaction residues. The coincident light particles were detected at forward angles, $\theta_{av} = 20^\circ$. Since the folding angle between two coincident fission fragments is related to the average linear momentum transfer to the heavy reaction residue, one can discriminate quasi-elastic peripheral reactions from more violent fusion-like collisions by placing appropriate gates on folding angles. The effectiveness of this reaction filter was demonstrated by the rather dramatic dependence of the energy spectra on folding angle. When fission fragments are emitted with large folding angles, the energy spectra of the coincident light particles exhibit a pronounced beam-velocity component. This component is reduced significantly when smaller folding angles (i.e. larger linear momentum transfers to the heavy reaction residue) are selected.

Correlation functions for coincident deuterons and α -particles exhibit a pronounced dependence on the total kinetic energy, $E_\alpha + E_d$, when they are gated by small folding angles (i.e. fusion-like collisions). This energy dependence is not observed for αd correlation functions gated on large folding angles (i.e. quasi-elastic peripheral collisions). Furthermore, two-particle correlations gated by small folding

angles exhibit larger maxima than those gated by quasi-elastic peripheral collisions. Increasing contributions from the decay of excited projectile residues were argued⁴⁹⁾ to account for the fact that inclusive two-particle correlations become more pronounced for higher total kinetic energies of the emitted particles. Our observations show the opposite effect.

Most likely, temporal effects cannot be neglected when interpreting the magnitude of the correlation function measured in the present experiment. Particles emitted from equilibrated reaction residues can be expected to be emitted at larger average time intervals than particles emitted from the early nonequilibrated stages of the reaction. Larger emission time scales will dampen the two-particle correlation functions. Particle emission from equilibrated heavy reaction residues contributes predominantly to the low energy portions of the energy spectra. Particle emission from equilibrated projectile residues can be enhanced by selecting quasi-elastic peripheral reactions and detecting the emitted particles at forward angles. In both cases, reduced correlations are observed. The selection of energetic particles emitted at larger angles or in fusion-like reactions should enhance contributions from the early nonequilibrated stages of the reaction. For this class of reactions, the measured correlations are most pronounced and should reflect more clearly the spatial localization during the early stages of the reaction.

Mean emission temperatures extracted from the relative populations of particle unbound states in ${}^5\text{Li}$ and ${}^6\text{Li}$ were found to be remarkably similar for quasi-elastic peripheral collisions and more violent fusion-like reactions. Perhaps even more surprising is the similarity of temperatures extracted for the present reactions to those extracted for ${}^{40}\text{Ar}$ induced reactions on ${}^{197}\text{Au}$ at $E/A = 60$ MeV. This similarity raises the immediate question whether the relative populations of states reach a saturation value corresponding to rather low emission temperatures of $T \approx 5$ MeV. Measurements at higher beam energies are clearly needed. At the same time, a better theoretical understanding of the final stages of the nuclear disassembly is needed. The assumption of local chemical equilibrium may be too crude an approximation for the relative populations of states; perturbations by final-state interactions between the emitted particles could be significant⁵⁰⁾. If the measured populations of states differed significantly from the primary ones the extracted temperatures could be inaccurate. Up to now, the sequential feeding of particle unbound states in ${}^5\text{Li}$ and ${}^6\text{Li}$ from higher-lying states has only been investigated^{41,42)} under the simplifying assumption that only *known* resonances are populated. These investigations predict only minor perturbations for the relative populations of the ${}^5\text{Li}$ states investigated in this experiment. However, the role of high-lying continuum states remains unclear and should be investigated in future.

This work was supported by the National Science Foundation under Grant No. PHY 83-12245. J.P. acknowledges the receipt of a fellowship of the Deutsche

Forschungsgemeinschaft (W. Germany) and W.G.L. acknowledges the receipt of a US Presidential Young Investigator Award.

References

- 1) G.D. Westfall, J. Gosset, P.J. Johansen, A.M. Poskanzer, W.G. Meyer, H.H. Gutbrod, A. Sandoval and R. Stock, *Phys. Rev. Lett.* **37** (1976) 1202
- 2) J. Gosset, J.I. Kapusta and G.D. Westfall, *Phys. Rev.* **C18** (1978) 844
- 3) J. Knoll, *Phys. Rev.* **C20** (1979) 773
- 4) B.V. Jacak, G.D. Westfall, C.K. Gelbke, L.H. Harwood, W.G. Lynch, D.K. Scott, H. Stöcker, M.B. Tsang and T.J.M. Symons, *Phys. Rev. Lett.* **51** (1983) 1846
- 5) R. Shyam and J. Knoll, *Nucl. Phys.* **A426** (1984) 606; *Phys. Lett.* **136B** (1984) 221; Erratum (1986), unpublished
- 6) D.J. Fields, W.G. Lynch, C.B. Chitwood, C.K. Gelbke, M.B. Tsang, H. Utsunomiya and J. Aichelin, *Phys. Rev.* **C30** (1984) 1912
- 7) J. Aichelin, *Phys. Rev. Lett.* **52** (1984) 2340
- 8) G.D. Westfall, B.V. Jacak, N. Anantaraman, M.W. Curtin, G.M. Crawley, C.K. Gelbke, B. Hasselquist, W.G. Lynch, D.K. Scott, M.B. Tsang, M.J. Murphy, T.J.M. Symons, R. Legrain and T.J. Majors, *Phys. Lett.* **116B** (1982) 118
- 9) P.J. Siemens and J.O. Rasmussen, *Phys. Rev. Lett.* **42** (1979) 880
- 10) W.A. Friedman and W.G. Lynch, *Phys. Rev.* **C28** (1983) 16, 950
- 11) H. Stöcker, A.A. Ogloblin and W. Greiner, *Z. Phys.* **A313** (1981) 259
- 12) S. Ban-Hao and D.H.E. Gross, *Nucl. Phys.* **A437** (1985) 643
- 13) D.J. Morrissey, W. Benenson, E. Kashy, B. Sherrill, A.D. Panagiotou, R.A. Blue, R.M. Ronningen, J. van de Plicht and H. Utsunomiya, *Phys. Lett.* **148B** (1984) 423
- 14) D.J. Morrissey, W. Benenson, E. Kashy, C. Bloch, M. Lowe, R.A. Blue, R.M. Ronningen, B. Sherrill, H. Utsunomiya and I. Kelson, *Phys. Rev.* **C32** (1985) 877
- 15) D.J. Morrissey, C. Bloch, W. Benenson, E. Kashy, R.A. Blue, R.M. Ronningen and R. Aryaeinejad, *Phys. Rev.* **C34** (1986) 761
- 16) J. Pochodzalla, W.A. Friedman, C.K. Gelbke, W.G. Lynch, M. Maier, D. Ardouin, H. Delagrange, H. Doubre, C. Grégoire, A. Kyanowski, W. Mittig, A. Péghaire, J. Péter, F. Saint-Laurent, Y.P. Viyogi, B. Zwieglinski, G. Bizard, F. Lefèbvres, B. Tamain and J. Québert, *Phys. Lett.* **161B** (1985) 275 177
- 17) J. Pochodzalla, W.A. Friedman, C.K. Gelbke, W.G. Lynch, M. Maier, D. Ardouin, H. Delagrange, H. Doubre, C. Grégoire, A. Kyanowski, W. Mittig, A. Péghaire, J. Péter, F. Saint-Laurent, Y.P. Viyogi, B. Zwieglinski, G. Bizard, F. Lefèbvres, B. Tamain and J. Québert, *Phys. Lett.* **161B** (1985) 275
- 18) J. Pochodzalla, C.K. Gelbke, W.G. Lynch, M. Maier, D. Ardouin, H. Delagrange, H. Doubre, C. Grégoire, A. Kyanowski, W. Mittig, A. Péghaire, J. Péter, F. Saint-Laurent, B. Zwieglinski, G. Blizard, F. Lefèbvres, B. Tamain, and J. Québert, Y.P. Viyogi, W.A. Friedman and D.H. Boal, *Phys. Rev.* **C35** (1987) 1695
- 19) C.B. Chitwood, C.K. Gelbke, J. Pochodzalla, Z. Chen, D.J. Fields, W.G. Lynch, R. Morse, M.B. Tsang, D.H. Boal and J.C. Shillcock, *Phys. Lett.* **172B** (1986) 27
- 20) H.M. Xu, D.J. Fields, W.G. Lynch, M.B. Tsang, C.K. Gelbke, M.R. Maier, D.J. Morrissey, J. Pochodzalla, D.G. Sarantites, L.G. Sobotka, M.L. Halbert, D.C. Hensley, D. Hahn and H. Stöcker, *Phys. Lett.* **182B** (1986) 155
- 21) R. Hanbury-Brown and R.Q. Twiss, *Nature* **178** (1956) 1046
- 22) G. Goldhaber, S. Goldhaber, W. Lee and A. Pais, *Phys. Rev.* **120** (1960) 300
- 23) E.V. Shuryak, *Phys. Lett.* **44B** (1973) 387
- 24) G.I. Kopylov and M.I. Podgoretskii, *Sov. J. Nucl. Phys.* **18** (1974) 336 (*Yad. Fiz.* **18** (1973) 656)
- 25) G.I. Kopylov, *Phys. Lett.* **50B** (1974) 472
- 26) F.B. Yano and S.E. Koonin, *Phys. Lett.* **78B** (1978) 556
- 27) S.E. Koonin, *Phys. Lett.* **70B** (1977) 43

- 28) H. Sato and K. Yazaki, in: High-energy nuclear interactions and properties of dense nuclear matter, ed. K. Nakai and A.S. Goldhaber, p. 340
- 29) D.H. Boal and J.C. Shillcock, *Phys. Rev.* **C33** (1986) 549
- 30) B.K. Jennings, D.H. Boal and J.C. Shillcock, *Phys. Rev.* **C33** (1986) 1303
- 31) F. Zarbakhsh, A.L. Sagle, F. Brochard, T.A. Mulera, V. Perez-Mendez, R. Talaga, I. Tanihata, J.B. Carroll, K.S. Ganezer, G. Igo, J. Oostens, D. Woodard and R. Sutter, *Phys. Rev. Lett.* **46** (1981) 1268
- 32) W.G. Lynch, C.B. Chitwood, M.B. Tsang, D.J. Fields, D.R. Klesch, C.K. Gelbke, G.R. Young, T.C. Awes, R.L. Ferguson, F.E. Obenshain, F. Plasil, R.L. Robinson and A.D. Panagiotou, *Phys. Rev. Lett.* **51** (1983) 1850
- 33) H.A. Gustafsson, H.H. Gutbrod, B. Kolb, H. Löhner, B. Ludewigt, A.M. Poskanzer, T. Renner, H. Riedesel, H.G. Ritter, A. Warwick, F. Weik and H. Wieman, *Phys. Rev. Lett.* **53** (1984) 544
- 34) C.B. Chitwood, J. Aichelin, D.H. Boal, G. Bertsch, D.J. Fields, C.K. Gelbke, W.G. Lynch, M.B. Tsang, J.C. Shillcock, T.C. Awes, R.L. Ferguson, F.E. Obenshain, F. Plasil, R.L. Robinson and G.R. Young, *Phys. Rev. Lett.* **54** (1985) 302
- 35) J. Pochodzalla, C.B. Chitwood, D.J. Fields, C.K. Gelbke, W.G. Lynch, M.B. Tsang, D.H. Boal and J.C. Shillcock, *Phys. Lett.* **174B** (1986) 36
- 36) Z. Chen, C.K. Gelbke, J. Pochodzalla, C.B. Chitwood, D.J. Fields, W.G. Lynch and M.B. Tsang, *Phys. Lett.* **186B** (1987) 280
- 37) J. Pochodzalla, C.K. Gelbke, C.B. Chitwood, D.J. Fields, W.G. Lynch, M.B. Tsang and W.A. Friedman, *Phys. Lett.* **175B** (1986) 275
- 38) C.K. Gelbke and D.H. Boal, *Prog. Nucl. Phys.* **19** (1987) 33
- 39) T.C. Awes, G. Poggi, S. Saini, C.K. Gelbke, R. Legrain and G.D. Westfall, *Phys. Lett.* **103B** (1981) 417
- 40) C.B. Chitwood, D.J. Fields, C.K. Gelbke, D.R. Klesch, W.G. Lynch, M.B. Tsang, T.C. Awes, R.L. Ferguson, F.E. Obenshain, F. Plasil, R.L. Robinson and G.R. Young, *Phys. Rev.* **C34** (1986) 858
- 41) D. Hahn and H. Stöcker, *Phys. Rev.* **C35** (1987) 1311
- 42) D.J. Fields, C.K. Gelbke, W.G. Lynch and J. Pochodzalla, *Phys. Lett.* **187B** (1987) 257
- 43) J. Pochodzalla, W.A. Friedman, C.K. Gelbke, W.G. Lynch, M. Maier, D. Ardouin, H. Delagrange, H. Doubre, C. Grégoire, A. Kyanowski, W. Mittig, A. Péghaire, J. Péter, F. Saint-Laurent, Y.P. Viyogi, B. Zwieglinski, G. Bizard, F. Lefèbvres, B. Tamain and J. Québert, *Phys. Lett.* **161B** (1985) 256
- 44) D.H. Boal and H. DeGuise, *Phys. Rev. Lett.* **57** (1986) 2901
- 45) B.B. Back, K.L. Wolf, A.C. Mignerey, C.K. Gelbke, T.C. Awes, H. Breuer, V.E. Viola, Jr. and P. Dyer, *Phys. Rev.* **C22** (1980) 1927
- 46) T.C. Awes, G. Poggi, C.K. Gelbke, B.B. Back, B.G. Glagola, H. Breuer and V.E. Viola, Jr., *Phys. Rev.* **C24** (1981) 89
- 47) M.A. Bernstein, W.A. Friedman, W.G. Lynch, C.B. Chitwood, D.J. Fields, C.K. Gelbke, M.B. Tsang, T.C. Awes, R.L. Ferguson, F.E. Obenshain, F. Plasil, R.L. Robinson and G.R. Young, *Phys. Rev. Lett.* **54** (1985) 402
- 48) M.B. Tsang, C.B. Chitwood, D.J. Fields, C.K. Gelbke, D.R. Klesch, W.G. Lynch, K. Kwiatkowski and V.E. Viola, Jr., *Phys. Rev. Lett.* **52** (1984) 1967
- 49) P.D. Bond and R.J. de Meijer, *Phys. Rev. Lett.* **52** (1984) 3201
- 50) D.H. Boal, *Phys. Rev.* **C30** (1984) 749